

Epsilon near zero metal oxide based spectrally selective reflectors

*Sraboni Dey**, *Kirandas P S*, *Deepshikha Jaiswal Nagar* and *Joy Mitra**

School of Physics, Indian Institute of Science Education and Research Thiruvananthapuram,
Kerala - 695551, India

*Email: srabonidey20@iisertvm.ac.in, j.mitra@iisertvm.ac.in

ABSTRACT

Epsilon near zero (ENZ) materials can contribute significantly to the advancement of spectrally selective coatings aimed at enhancing efficient use of solar radiation and thermal energy management. Here, we demonstrate a subwavelength thick, multilayer optical coating that imparts a spectrally “step function” like reflectivity onto diverse surfaces, from stainless steel to glass, employing indium tin oxide as the key ENZ material. The coating, harnessing the ENZ and plasmonic properties of nominally nanostructured ITO along with ultrathin layers of Cr and Cr₂O₃ show 15% reflectivity over the visible to near-infrared and 80% reflectivity (and low emissivity) beyond a cut-in wavelength around 1500 nm, which is tunable in the infrared. A combination of simulations and experimental results are used to optimize the coating architecture and gain insights into the relevance of the components. The straightforward design with high thermal stability will find applications requiring passive cooling.

KEYWORDS: *Spectrally selective coatings, engineering optical properties, epsilon-near-zero*

1. INTRODUCTION

Solar radiation management, a key component of sustainable energy generation, is an area of wide topical interest wherein spectrally selective coatings form an important domain of research [1, 2]. Engineering spectral selectivity of surfaces through coatings offers an opportune way to maximize effective utilization of incident and radiated energies. This discussion focuses on realizing a coating exhibiting idealized step-function-like reflectivity (R), characterized by high absorption in the visible and high reflectance and low emissivity in the infrared, separated by a cut-in wavelength λ_o . Design and fabrication of such coatings that are durable, cost-effective and scalable, ensuring compatibility with diverse surfaces remain open challenges. Strategies for inducing such selectivity have broadly centered on assembling the right materials (semiconductors, metals and dielectrics) in conducive form factors like multilayers or composites with two and three-dimensional texturing [3, 4]. The increasing ability to engineer hybrid materials with sub-wavelength scale layering [5] and structuring [6] has broadened the scope of tailoring spectral selectivity. Fundamentally, the above schemes rely on the physics of light-matter interactions and engineering radiative vs. non-radiative modes, as realized in photonic crystals [7, 8] and optical metamaterials [9, 10]. Interestingly, non-radiative regimes are also realized in continuous media such as the epsilon near zero (ENZ) materials, near their ENZ wavelength (λ_{ENZ}).

Conducting oxides like Al-doped ZnO, indium tin oxide, doped CdO etc. [11, 12] harbor ENZ regimes that originate from their free electron response. As $\lambda \rightarrow \lambda_{ENZ}$, the real part of their relative permittivity ($\epsilon(\omega) = \epsilon' + i\epsilon''$), $\epsilon' \rightarrow 0$ and the λ_{ENZ} demarcates a dielectric to metallic transition in terms of their optical properties. Consequently, ENZ systems sustain non-radiative modes around λ_{ENZ} and ultra-thin layers ($t \sim 10$ nm) show perfect absorption (PA) with strong directional preference [13]. Spectrally, PA is realized at wavelengths $\lambda_{PA} \lesssim \lambda_{ENZ}$ and is coupled

with excitation of the ENZ modes accompanied by extreme field amplification and confinement [14]. Further, the metallic response of the ENZ thin films for $\lambda > \lambda_{ENZ}$, ensures high reflectivity ($R \rightarrow 1$) at longer wavelengths, which together with $R \sim 0$ for PA enables a niche application of ENZ thin films in developing spectrally selective coatings of sub-wavelength dimensions.

Coatings that impart a step-function-like reflectivity (SFR) to flat surfaces are of vital interest in solar energy conversion[15,16], thermal management[17,18], radiative cooling[19], smart windows [20] and related areas. The optical properties of surfaces like stainless steel (SS), Si, glass, Cu etc. that are used across diverse platforms have been variously modified to impart SFR, as summarized in table 1. Typically, the samples (coated substrate) are dominantly absorbing (or transmissive) in the visible to near-infrared ($\lambda < \lambda_o$) and become highly reflecting above λ_o . The latter minimizes radiative energy loss by minimizing thermal emissivity, for $\lambda > \lambda_o$, and thus a sharper transition from low to high R across the λ_o increases the overall efficiency of the coating, in terms of thermal emissivity.

Table 1: Details of coatings that impart spectrally selective and step function like variation in Reflectivity on various surfaces.

Material on Substrate	Absorptivity (VIS/NIR)	Emissivity (E) (IR)	Sharpness of transition ($\Delta\lambda$) (nm)	Refs.
Cr/SiO ₂ /Cr on Si	0.99	-	-	[21]
W/WAIN/WAlON/Al ₂ O ₃ on SS	0.90	0.15	~2000	[22] [23]
TiAlC/TiAlCN/TiAlSiCN/TiAlSiCO/TiAlSiO on SS	0.961	0.07	~1000	[24]
3 -SiC-W nanocomposite layers on Si	0.95	0.05	~3000	[25]
Structured graphene metamaterial on Cu *	~0.90	~0.04	~1800	[26]
ITO NS /ITO / Cr/ Cr ₂ O ₃ on SS and Glass *	0.87 (SS)	0.18(SS)	~400	This work
Cu/Al ₂ O ₃ /Cr/SiO ₂ /Cr/SiO ₂ on Glass and Si	0.954	0.196	~2000	[27]
Au/NiCr-MgF ₂ (HMFV)/ NiCr-MgF ₂ (LMVF)/MgF ₂ on SS	0.976	0.045	~3500	[16]
Multilayer graphene + TiN based metamaterial *	0.88	0.03	~2000	[28]

SiO ₂ / Al ₂ O ₃ / ZrB ₂ / Al ₂ O ₃ / ZrB ₂ / ZrB ₂ / Al ₂ O ₃ / ZrB ₂ on SS and Si	0.96	0.16	~2000	[29]
W/WAlSiN/SiON/SiO ₂ on SS and Si	0.955	0.10	~2000	[30]
Multilayer reduced graphene oxide on Al *	0.92	0.04	~1,750	[31]
CrN(H)/CrN(L)/CrON/Al ₂ O ₃ on SS	0.93	0.14	~3000	[32]
Pt/ TiO ₂ / Al on SS *	0.90	-	-	[33]
Black chrome/ITO/SiO ₂ on SS	0.90	0.4	~1200	[34]

*Tunability demonstrated

However, these coatings involve significant complexity in growth, optimization and incorporation into a coating format, and a majority of their spectral response exhibits a wide low to high R crossover regime, $\Delta\lambda \gtrsim 2 \mu m$. Thus narrowing $\Delta\lambda$ to lower emissivity, improving stability and spectral tunability are challenges that form the basis of ongoing research in the area.

Leveraging the novel optical properties of ENZ materials like ITO, the primary aim here has been to demonstrate (i) SFR on opaque surfaces like SS, (ii) wide-angle SFR response and be of (iii) sub-wavelength thickness with nominal nano-structuring and for performance comparison, the same coating has been tested on a transparent material like glass. The design of meta-surfaces, broadband absorbers, and spectrally selective absorbers and reflectors using ITO have been studied in recent times [34, 35, 36, 37, 38]. Importantly, ITO has shown significant advantages compared to other transparent conducting oxides (TCOs) owing to its robustness in moist air, thermal stability, surface smoothness, mechanical stability and simple fabrication process [39] thereby encouraging its usage in spectral selective optical systems. Experimentally measured optical and thermal properties of coated surfaces, in conjunction with simulated responses, are used to comprehend the physics of surface engineering, where an ENZ material (ITO) imparts spectrally selective, wide-angle optical properties to commercially relevant substrates like opaque SS and glass from the visible to IR. The developed coating is a multi-layer of thin films of ITO/Cr/Cr₂O₃/substrate. Further, an elementary nanostructured grating of ITO (Fig 1) is shown to

further tune λ_o beyond the λ_{ENZ} of the ENZ material. The (wide angle $0^\circ - 60^\circ$), “step function” like spectral response is demonstrated for both flat and nanostructured coatings for λ_o around 1500 nm along with a sharp $\Delta\lambda \sim 400$ nm. Finally, control of λ_o via changing the free electron density of ITO is demonstrated. The coating structure is readily adapted as a traditional solar absorber for $\lambda_o \sim 2500$ nm and the concept is indeed functional in other spectral ranges with relevant ENZ materials.

2. RESULTS AND DISCUSSION

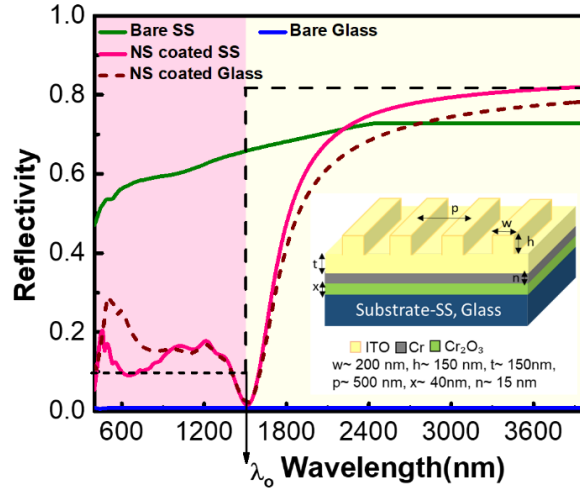


Figure 1. Spectral reflectivity showing the ideal “step function” like response (dashed line) along with the simulated response for bare SS and glass and with nanostructured coating. Inset shows schematic of the nanostructured coating.

Fig. 1 shows the schematic of the multilayer coating with NS, and the ideal SFR (dashed line) along with R for bare SS and glass and those simulated using p -polarized light with NS coating on both substrates, averaged over incident angles from $0^\circ - 60^\circ$. Bare SS shows a monotonic variation in R from 0.5 – 0.7, while glass displays complete transparency. The NS coating radically changes the reflectivity of both the opaque and transparent substrate with their simulated R vs. λ displaying SFR response.

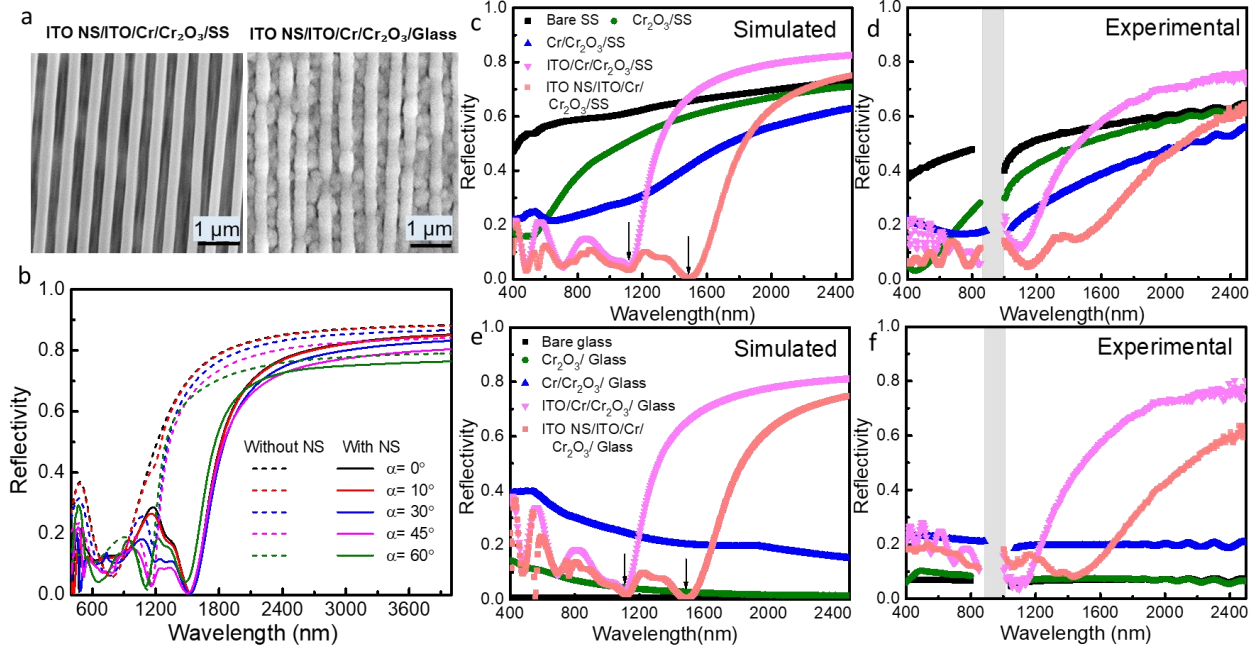


Figure 2(a) SEM images of ITO NS/ITO/Cr/Cr₂O₃ on SS and glass; (b) Simulated reflectivity spectra for SS coated with and without NS coating at selected angles for $\lambda_{ENZ} = 1220 \text{ nm}$; Simulated and Experimental reflectivity spectra of- (c)(d) Bare SS, Cr₂O₃ on SS, Cr/ Cr₂O₃/SS, ITO/Cr/ Cr₂O₃/SS, ITO NS/ITO/ Cr/ Cr₂O₃/SS; (d)(e) Bare BK7 glass, Cr₂O₃ on Glass, Cr/ Cr₂O₃/Glass, ITO/Cr/Cr₂O₃/Glass, ITO NS/ ITO/ Cr/Cr₂O₃/Glass. Down arrows denote the λ_o with and without NS. The shaded region in experimental plots-noise from the spectrometer.

Fig. 2a shows the secondary electron images of the coated substrates, showing the grating NS on each. Morphological features of the bare substrates and after deposition of each layer are shown in SI Section 2 (figs. S3 and S4), with the latter demonstrating large area patterning of the substrates. Figs. 2(c-d) show the simulated and experimental reflectivity spectra for SS as it is coated by the various components of the multilayer, and figs. 2(e-f) show the same for glass – recording evolution of reflectivity. They demonstrate quantifiable agreement between the simulated and experimental results and elucidate the role of individual layers in realizing the final response. Note that coatings with flat ITO and NS ITO, both show the SFR response with different λ_o . In all cases the λ_o is taken to be the wavelength with the smallest reflectivity before transition. ITO is a low-loss dielectric for $\lambda < \lambda_{ENZ}$, thus the low R at shorter λ (fig 1) arise primarily from

the optical properties of the underlying layers Cr/Cr₂O₃/substrate. On SS, this structure realizes a Fabry Perot cavity for *p*-polarized light at wavelengths below 500 nm, with the reflective Cr and SS increasing the effective interaction of light with these lossy materials, which contributes to overall lowering of *R*. The low loss, non-dispersive nature of Cr₂O₃ from 400 – 4000 nm [40] allows tuning the absorption by optimizing the thickness of the Cr layer. The Cr layer with optimized thickness of 15 nm is critically responsible for balancing the trade-off between light penetration and absorption, while ensuring its integrity as a uniform optical layer. ITO undergoes a dielectric to metal transition at λ_{ENZ} and progressively becomes more reflective for $\lambda > \lambda_{ENZ}$ resulting in the high *R* at longer λ . For wavelengths just below λ_{ENZ} , in the ENZ regime (where $(\epsilon') > 0$ and $n < 1$) ITO thin films also exhibit perfect absorption (PA) thereby reducing its $R \sim 0$. Thus, reflectivity for the coating without NS (fig 2b) starts increasing for $\lambda > \lambda_{ENZ}$ with $\lambda_o \approx \lambda_{ENZ}$. The relevance of the NS ITO grating is evidenced in the simulated plots of *R* shown in fig. 2b. Both with and without NS the *R* saturates to $\sim 80\%$ above 2000 nm however for coatings with NS, $\lambda_o \sim 1500$ nm is red-shifted from λ_{ENZ} and is determined by the grating dimensions. The final dimensions of each element are optimized via simulations to deliver the desired spectral response as discussed in Section 1 of SI.

In spite of the correlation between the experimentally measured reflectivity and the simulations some major differences are apparent. The measured *R* is systematically lower than the simulated value, across each layer and the $\Delta\lambda$ observed experimentally is higher than that predicted in the simulations. These departures primarily originate from scattering due to roughness of each of the deposited films and finally structuring. Importantly, though the predicted and observed values of λ_o for coatings with and without NS are in agreement with each other. It is also interesting that the coatings render comparable reflectivity to diverse substrates like glass and SS, which highlights

the determining role played by the multilayer. The glass coated substrate shows low reflectivity and transmittivity ($<20\%$, see SI Section 3, fig. S7) in the visible for $\theta_{in} = 0^\circ - 90^\circ$, which benefits from the refractive index contrast of 1.5 (glass) and 2.2 (Cr_2O_3). It also enables total internal reflection for $\theta_{in} > 42^\circ$ thus, increases interaction with the lossy Cr layer leading to absorption and suppressing reflectivity in the visible regime over a wide angular regime. In spite of having low reflectivity in the visible, the nanostructured portions show structural colours as evident in the optical images around 45° angles (SI section 4, fig S8).

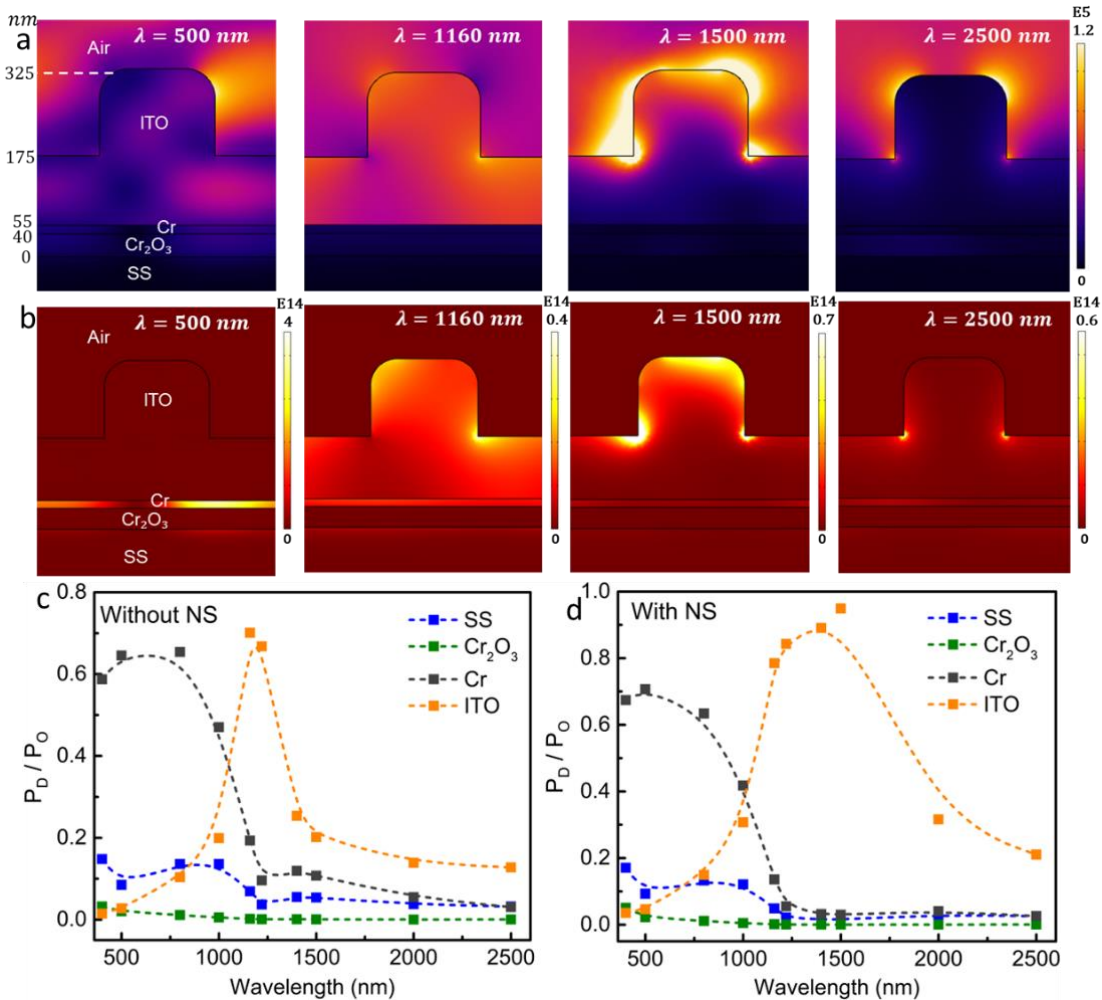


Fig 3. (a) Simulated electric field (V/m) and (b) dissipated power density (W/m^3) across the system at selected wavelengths; Spectral variation of power dissipated as a fraction of incident power, across the various layers (c) without nanostructures and (d) with nanostructures.

The simulations offer further insights into the role of each component of the multilayer coating in eliciting the overall response. Figs. 3(a-b) plot the calculated electric field ($|\mathbf{E}|$) and power dissipation density ($P_D = 1/2(\omega\epsilon''|\mathbf{E}|^2)$) along the cross section of the NS coating on SS, at selected wavelengths. Figs. 3(c-d) show the spectral variation of net power dissipated ($\int P_D dv$), in the various layers for coatings with and without NS. For $\lambda < \lambda_{ENZ}$, P_D is highest ($\sim 70\%$) in the Cr layer, the remaining radiation being absorbed in SS. Dissipation in ITO increases as $\lambda \rightarrow \lambda_{ENZ}$ and is highest around λ_{ENZ} since $\epsilon' \rightarrow 0$, which maximizes the \mathbf{E} field in ITO and thus P_D . Dissipation decreases at longer λ due to the increasing reflectivity of ITO thus decreasing field penetration. For the coating with the NS λ_o red-shifts to 1500 nm, around 300 nm beyond λ_{ENZ} and dissipation remains high in ITO between $\lambda_{ENZ} - \lambda_o$. The \mathbf{E} field plots 1500 nm show signatures of dipolar resonances originating from the plasmonic response of the ITO NS, dimensions of which are comparable to the λ . Also, the calculated \mathbf{E} field is enhanced in the vicinity of NS compared to the flat coating as shown in SI section 5 Fig S9, indicative of the resonances in NS. They cumulatively impart high absorbance to the NS ITO coating between $\lambda_{ENZ} - \lambda_o$ and are responsible for red-shifting λ_o showing that the narrow $\Delta\lambda \sim 400$ nm transition width across the wide incidence angle is achievable only with the NS. Note that the reflectivity is also reduced in the visible with the introduction of the NS, as validated by the experimental results in fig. 2d and fig. 2f. The above features demonstrate the dominant role played by the properties of ITO in achieving the SFR response and contextualize the relevance of the NS.

The λ_{ENZ} of ITO which crucially controls the λ_o of the coatings is determined primarily by the electron density (N_e) of ITO, thus varying N_e systematically changes λ_{ENZ} [41,42,43,44] and λ_o . N_e is readily tuned in ITO by altering the density of oxygen vacancies (N_{VO}) via annealing in various O_2 partial pressures [41]. Annealing in the ambient decreases N_{VO} and consequently N_e

which red-shifts the λ_{ENZ} and λ_o as shown in fig. 4a and fig. 4c. Here, both for SS and glass substrates the reflectance spectra of the as deposited coating exhibits $\lambda_o \sim 1220 \text{ nm}$, which red-shifts from 1220 nm – 1580 nm upon annealing at 350°C for 10 mins as tabulated in SI section 6, Table S1 and S2. Fig. 4b and fig. 4d show the corresponding simulated spectra keeping all material parameters unchanged except decreasing N_e , which decreases from $1.05 \times 10^{21}/\text{cc}$ to $6.62 \times 10^{20}/\text{cc}$. These results show that the coating is tunable yet thermally stable up to temperatures like 300°C . The calculated emissivity for the NS coated SS substrate, obtained by integrating the spectral response shows a low value of 0.2 in the IR with wide angular tolerance, along with high absorptivity ~ 0.8 over the visible to NIR, as discussed in SI section 7. The emissivity ~ 0.2 , calculated over the IR ($\lambda > \lambda_o$) is indicative of the coating's efficiency in minimizing the radiative energy loss in the IR.

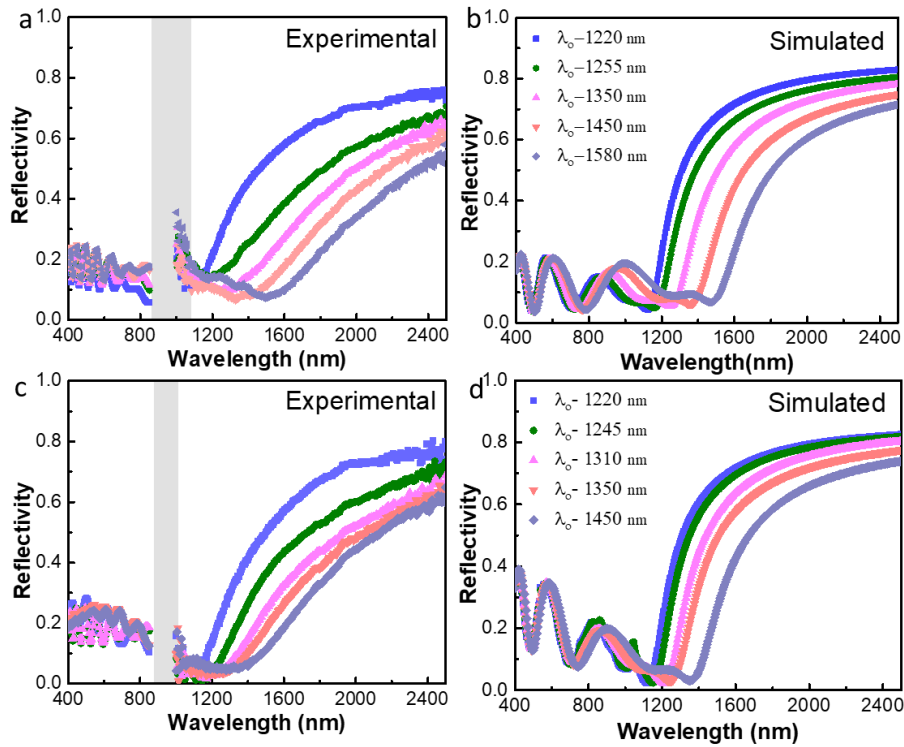


Figure 4. Experimental and Simulated reflectivity spectra of (a)(b) ITO/ Cr/ Cr₂O₃/SS; (c)(d) ITO/ Cr/ Cr₂O₃/Glass on annealing over certain time periods at 350°C . Shaded region in experimental plots-noise from the spectrometer.

The novelty of the coating's design and applicability in imparting the step function like reflectivity onto diverse surfaces is elucidated by the plot in SI fig. S11, which shows a SFR response (simulated R vs. λ) even for a free hanging coating i.e. with vacuum as the substrate. It demonstrates that the bulk of the response arises solely due to the coating and is minimally dependent on the optical properties of the substrate. However, the morphology of the substrate is still of relevance which needs to be optically flat to enable the grating nanostructure to perform as predicted in the IR.

3. Conclusion

In summary, we have developed a wide-angle, spectrally selective reflector coating that imparts step function like reflectivity on diverse substrates like SS and glass based on a straightforward design consisting of a tri-layer subwavelength thick Cr_2O_3 , Cr and ENZ thin film of ITO and a nanostructured grating. The average reflectivity over the entire visible and NIR $\lambda < 1500$ nm is $\sim 15\%$ and thereafter becomes highly reflecting with reflectivity $\sim 80\%$. A combination of optical characterization and numerical simulations have been used to examine the role of individual layers in the integrated coating. Spectral variation in the calculated power dissipation across the layers elucidates the role of each layer, demonstrating the confinement of the electric field in the SS- Cr_2O_3 -Cr layers, which uniformly suppresses reflectivity and maximizes absorption in the visible to NIR regime. The epsilon near zero property of ITO is exploited not only to impart strong reflectivity in the IR, but its nanostructured morphology is shown to improve the step function like reflectivity. Finally, the easy tunability of ITO's λ_{ENZ} via thermal annealing is shown to systematically shift the overall spectral response of the coating in the IR and this is perhaps the first demonstration of spectral tunability of a coating utilizing an ENZ material. Such a mechanism of obtaining tunable spectral selectivity over optically diverse substrates (opaque SS and

transparent glass) is promising in the field of energy management and demonstrates that the design ideas may be translated to other ENZ materials across other spectral regimes. Finally, this CMOS-compatible fabrication based on thin-film coatings and elemental nanostructuring is capable of achieving wide-angle, spectrally selective behavior offering a robust and cost-effective solution in optical engineering.

4. Materials and Methods

The multilayer structures were optimized in terms of the material properties and physical dimensions using finite element method modelling with 3D simulations conducted in the Wave Optics Module of COMSOL[®] Multiphysics 5.3a. The optimization scheme yielded the best optical response of the system considering feasibility of fabrication and experimental verification of the samples. It minimizes reflectance over the visible and maximizes reflectance above the cut-in wavelength (λ_o) with a straightforward fabrication protocol. The simulations were carried out in the range 400 – 4000 nm though the experimental verification is limited to 2500 nm. The optical properties of the materials were taken from the literature [40,45,46], with the Drude model used to determine that of ITO as a function of three parameters, carrier concentration N_e , scattering parameter γ and back ground permittivity ϵ_∞ . The typical values of the parameters (N_e , γ and ϵ_∞) follow those from a previous publication [41] from the group. The details of the model geometry and its optimization are given in the supporting information (section 1).

Sample fabrication

Polished stainless steel (SS) substrates (~7 mm x 7 mm x 0.5 mm, MTI, USA) and NBK7 glass substrates (~7 mm x 7 mm x 1 mm) were cleaned thoroughly using acetone, isopropyl alcohol and finally with DI water. 40 nm Cr was thermally evaporated on to the substrates at ~ 0.5 Å/s. The films were annealed at 600°C for 2 hours in the ambient to form Cr₂O₃, verified by XRD, EDX spectroscopy (EDS) and Raman spectroscopy, as shown in SI section 2. Subsequently, the samples

were coated with 15 nm Cr (thermal evaporation) followed by coating ITO (RF sputtering) of variable thickness from 150 – 350 nm. Chamber pressure for all depositions were maintained at lower than 2×10^{-6} mbar. ITO nanostructures of ~ 200 nm width and ~ 500 nm periodicity were patterned using electron beam lithography (Raith Pioneer 2) using 10 wt% PMMA resist. Lithographed samples were developed in a solution of methyl isobutyl ketone (MIBK) and isopropyl alcohol (IPA) in 1:3 volumetric ratio for 10 s followed by IPA wash for 10 s. Finally, ~ 150 nm ITO was sputter coated onto the patterned substrates with lift-off using warm acetone to yield the grating structure. Finally, the nanostructures samples were annealed using rapid thermal annealer (Mini Lamp Annealer-MILA 5000) for 15 minutes at 450°C in O_2 lean atmosphere ($\sim 10^{-6}$ mbar pressure), which yielded ITO with $\lambda_{ENZ} \sim 1220$ nm.

Material and optical Characterization

Morphological characterization was conducted using Nova Nano SEM 450 field emission scanning electron microscope (SEM) coupled with an Apollo X energy dispersive x-ray analysis (EDS) system. X-ray diffraction (XRD) studies were performed with $\text{Cu } K_\alpha = 1.540 \text{ \AA}$ at 45 kV (Empyrean, PANalytical). Raman spectra was obtained using a HORIBA Xplora Plus Raman setup with 532 nm laser excitation. Atomic force microscopy images were taken using a Bruker Multimode 8 AFM. Reflectance spectra were obtained in the range of 400 – 2500 nm (Perkin Elmer Lambda 950) using the Universal Reflectance Accessory module as well as the 60 mm Integrating Sphere module.

5. Author's Contribution

SD performed experiments and simulations. KPS and SD performed sputtering experiments. JM supervised the project. SD and JM analyzed data and wrote the manuscript with inputs from all the authors.

6. Acknowledgement

The authors thank Dr. S Kumaragurubaran, IISER TVM for the use of experimental facilities. SD acknowledges useful discussions with Dr. Ben Johns, IISER Mohali. The authors acknowledge ISTEM, Government of India, for access to the COMSOL Multiphysics software and financial support from SERB, Government of India (No. CRG/2023/006878). SD acknowledges a PhD fellowship from DST INSPIRE.

Notes

There are no conflicts to declare.

Supporting information

S1. Theoretical Modelling

S1.1 Model Details

The finite element method is Maxwell's solver and a widely used numerical simulation approach for determining electromagnetic properties. A unit cell of the investigated system was designed in COMSOL 5.3a as shown in Fig.S1 and was simulated using periodic boundary conditions.

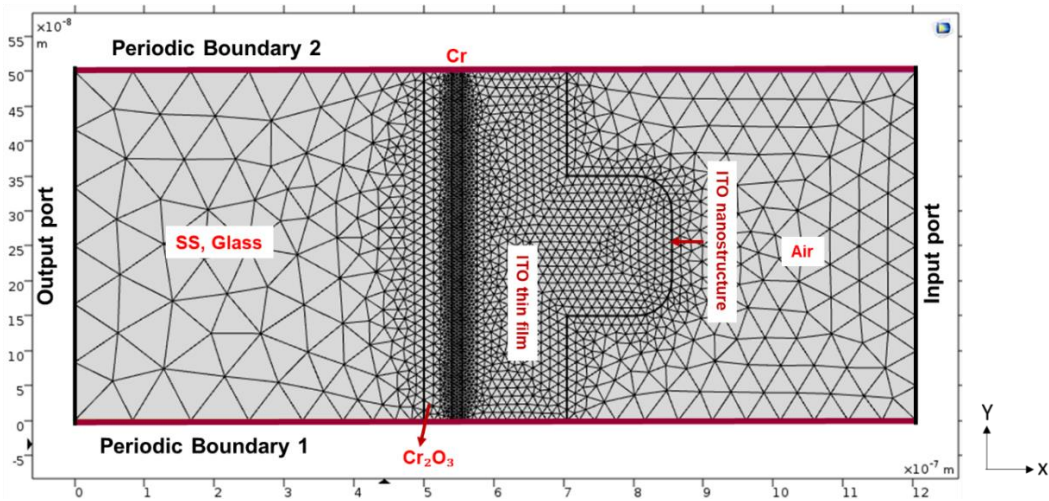


Figure S1: Cross sectional view of a unit cell designed in Wave optics module of COMSOL Multiphysics 5.3a

Two periodic ports were used where one was used to launch the incident wave and the other to collect the transmitted wave. Simulations were conducted using p-polarized light at selected angle of incidence and the reflectivity (R) was calculated. SS being a completely opaque substrate, the transmission through the system was zero.

S1.2 Optimization details of the nanostructure

The geometric dimensions of the nanostructures (NS) (width, height), as well as the periodicity of the array, were optimized systematically in COMSOL while developing the spectrally selective system. The width was varied keeping the height fixed, the height was varied keeping the width fixed and finally, the periodicity (centre to centre distance) was varied keeping the width and height fixed. Figure S2. shows that the nanostructure with ~ 200 nm width and ~ 150 nm height with ~ 500 nm periodicity helps to achieve the typical “step function” like reflectivity.

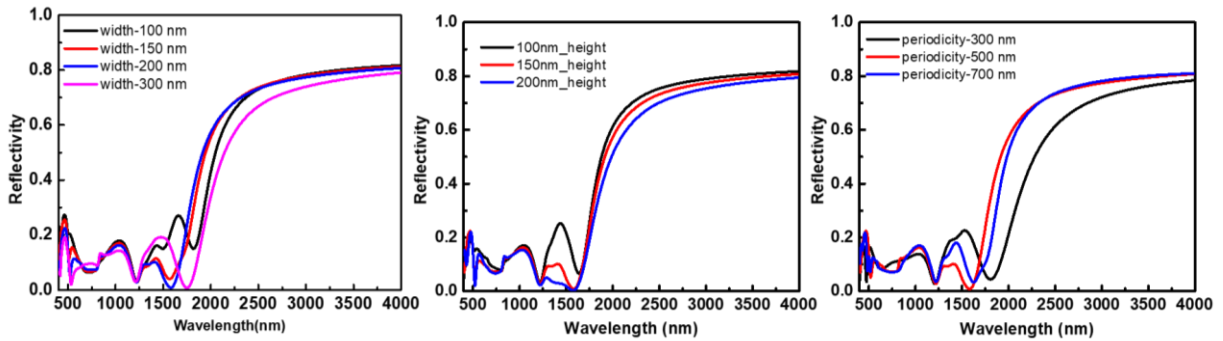


Figure S2(a) Simulated reflectivity plots for different width (100 nm, 150 nm, 200 nm, 300nm) of the NS, (b) different height (100 nm, 150 nm, 200 nm) of the NS, (c) different periodicity (300 nm, 500 nm, 700 nm) of the NS array.

S2. Material and morphological characterization

S2.1 Scanning electron microscopy (SEM)

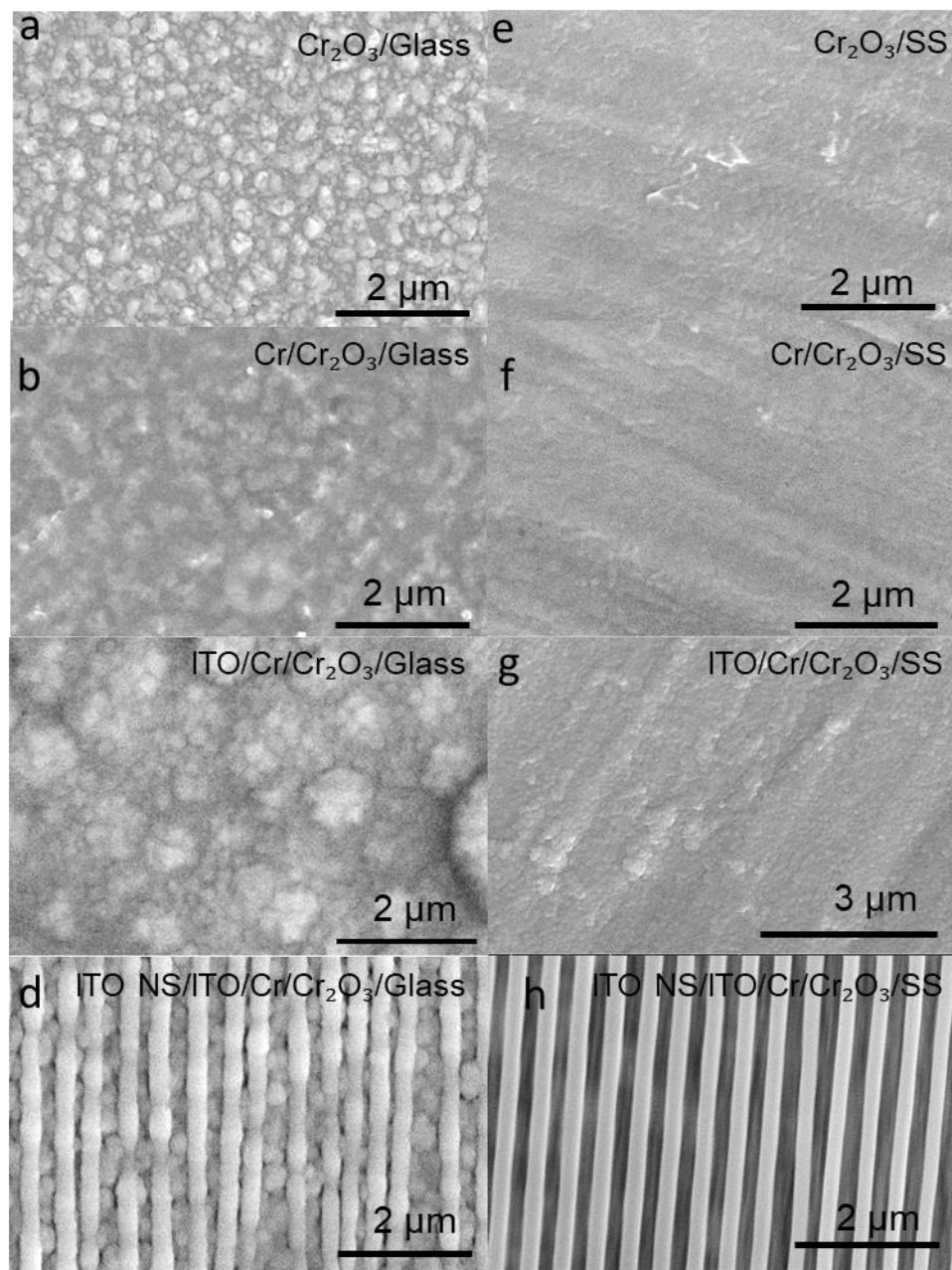


Figure S3. SEM images of the substrates after deposition of each layer, (a) Cr_2O_3 , (b) $\text{Cr}/\text{Cr}_2\text{O}_3$ (c) $\text{ITO}/\text{Cr}/\text{Cr}_2\text{O}_3$ (d) $\text{ITO NS}/\text{ITO}/\text{Cr}/\text{Cr}_2\text{O}_3$ on glass, (e) Cr_2O_3 , (f) $\text{Cr}/\text{Cr}_2\text{O}_3$, (g) $\text{ITO}/\text{Cr}/\text{Cr}_2\text{O}_3$, (h) $\text{ITO NS}/\text{ITO}/\text{Cr}/\text{Cr}_2\text{O}_3$ on SS.

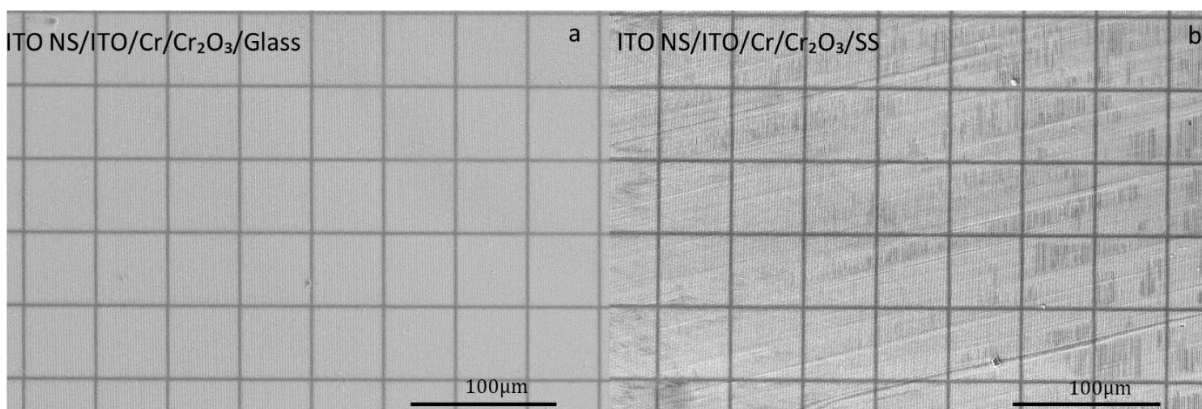


Figure S4. Large area SEM Images of the final multi-layered sample on (a) Glass substrate, (b) SS substrate

S2.1 Energy dispersive spectroscopy (EDS), X-ray Diffraction (XRD) and Raman spectroscopy.

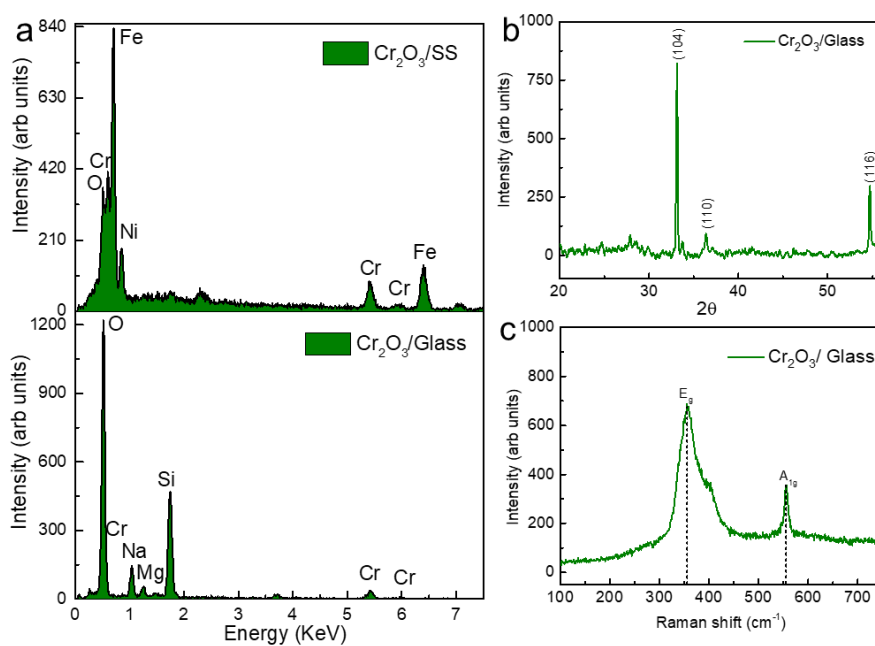


Figure S5 (a) EDS spectra of Cr₂O₃ on SS and glass, (b) XRD of Cr₂O₃ on glass, (c) Raman spectra of Cr₂O₃ on glass

S2.3 Surface characterization using atomic force microscopy (AFM)

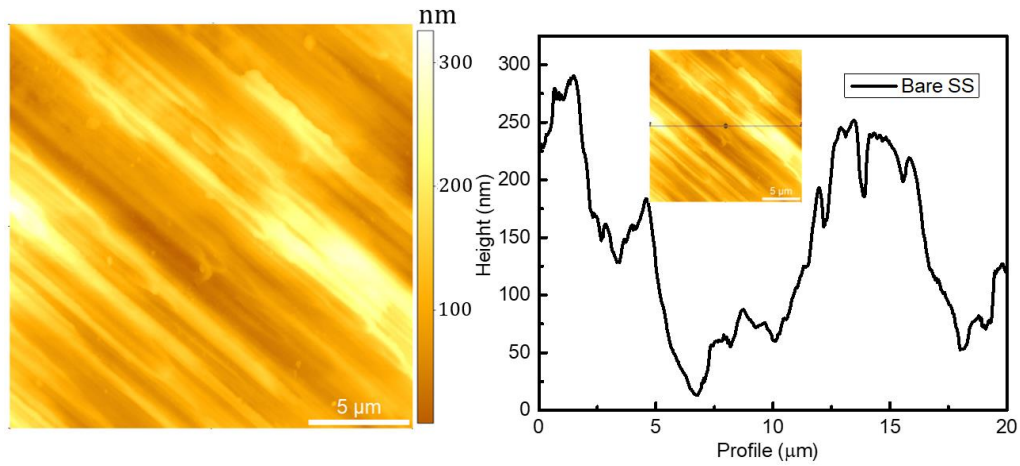


Figure S6. AFM topography of bare SS with the line-scan showing the height variation. The polished SS substrate shows significantly higher rms roughness (~ 120 nm) than the BK7 glass (roughness < 3 nm), estimated over $20 \times 20 \mu\text{m}^2$ areas. The average roughness of bare SS was calculated to be 118.44 nm.

S3. Transmission for the multilayer coating on glass substrate

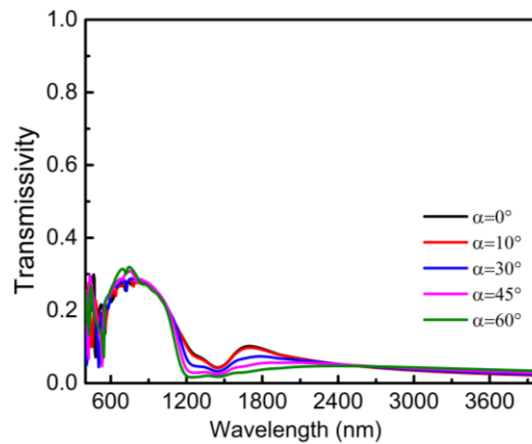


Figure S7. Transmissivity of the multilayer coating on glass substrate.

S4. Optical images of the final samples showing structural colours.

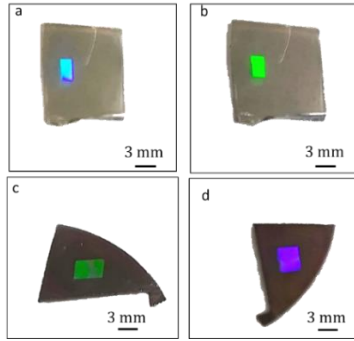


Figure S8. Optical images of the spectrally selective reflector on (a,b) glass substrate captured from different angles; (c,d) SS substrate captured from different angles. Different colours on the samples demarcate the nanostructured portion.

S5. Nanostructure resonance

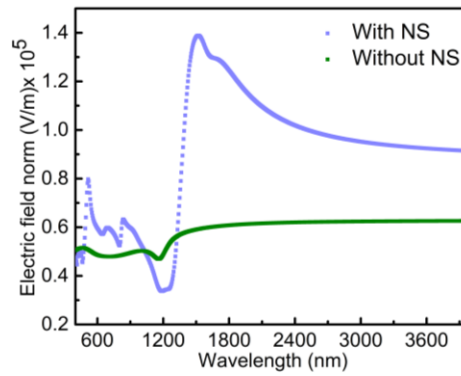


Figure S9. Simulated electric field magnitude (V/m) in the vicinity of NS and flat ITO without NS.

S6. Tuning of λ_{ENZ}

Annealing time (minutes)	0	10	20	24	30
λ_{ENZ} (nm) obtained	1220	1255	1350	1450	1580

Table S1: Annealing of multilayer on SS in ambient pressure conditions

Annealing time (minutes)	0	10	20	30	40
λ_{ENZ} (nm) obtained	1220	1245	1310	1350	1450

Table S2: Annealing of multilayer on glass in ambient pressure conditions

S7. Calculation of absorptivity (A) and Emissivity(E)

The absorptivity(A) and emissivity (E) of the coating on SS substrate was calculated using the equations 1 and 2 respectively.

$$A = \frac{\int_{0.4 \mu m}^{1.5 \mu m} (1 - R(\theta, \lambda)) I_s(\lambda, T) d\lambda}{\int_{0.4 \mu m}^{1.5 \mu m} I_s(\lambda, T) d\lambda} \quad [1]$$

$$E = \frac{\int_{2 \mu m}^{4 \mu m} (1 - R(\theta, \lambda)) I_b(\lambda, T) d\lambda}{\int_{2 \mu m}^{4 \mu m} I_b(\lambda, T) d\lambda} \quad [2]$$

I_s is the solar radiation spectrum, I_b is the blackbody radiation spectrum at 300 K and R is the calculated reflectivity at a particular angle θ and wavelength λ .

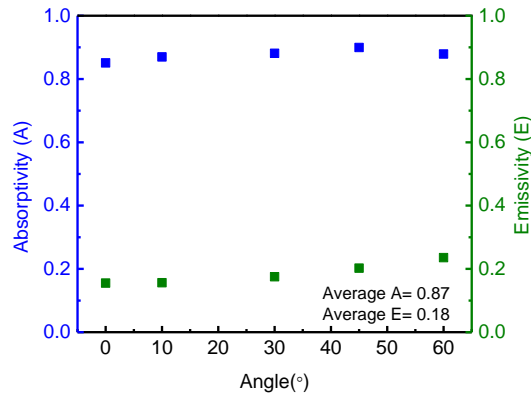


Fig S10. Variation of Calculated absorptivity and emissivity of multilayer on SS with angle

S8. Role of the substrate

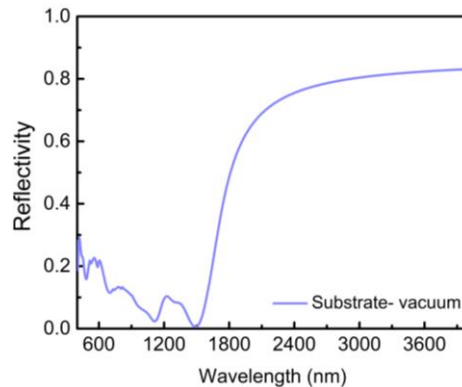


Fig S11. Simulated reflectivity of the spectrally selective coating at 45° with vacuum as the background substrate.

References

1. Li, Y., Lin, C., Huang, J., Chi, C., & Huang, B. (2021). Spectrally Selective Absorbers/Emitters for Solar Steam Generation and Radiative Cooling-Enabled Atmospheric Water Harvesting. *Global Challenges*, 5(1), 2000058.
2. Traverse, C. J., Pandey, R., Barr, M. C., & Lunt, R. R. (2017). Emergence of highly transparent photovoltaics for distributed applications. *Nature Energy*, 2(11), 849–860.
3. Tervo, E. J., & Steiner, M. A. (2022). Semiconductor-dielectric-metal solar absorbers with high spectral selectivity. *Solar Energy Materials and Solar Cells*, 240, 111735.
4. Cao, F., McEnaney, K., Chen, G., & Ren, Z. (2014). A review of cermet-based spectrally selective solar absorbers. *Energy and Environmental Science*, 7(5), 1615–1627.
5. Kecebas, M.A.; Menguc, M.P.; Kosar, A.; Sendur, K.(2020). Spectrally selective filter design for passive radiative cooling. *JOSA B*, 37, 1173–1182.
6. Khodasevych, I.E.; Wang, L.; Mitchell, A.; Rosengarten, G. (2015). Micro and nanostructured surfaces for selective solar absorption. *Adv. Opt. Mater.*, 3, 852–881.
7. Rinnerbauer, V.; Lenert, A.; Bierman, D.M.; Yeng, Y.X.; Chan, W.R.; Geil, R.D.; Senkevich, J.J.; Joannopoulos, J.D.; Wang, E.N.; Soljačić, M. (2014). Metallic photonic crystal absorber-emitter for efficient spectral control in high-temperature solar thermophotovoltaics. *Adv. Energy Mater.* 4, 1400334.
8. Celanovic, I.; Jovanovic, N.; Kassakian, J. (2008) Two-dimensional tungsten photonic crystals as selective thermal emitters. *Appl. Phys. Lett.*, 92, 193101.
9. Wang, H.; Sivan, V.P.; Mitchell, A.; Rosengarten, G.; Phelan, P.; Wang, L. (2015) Highly efficient selective metamaterial absorber for high-temperature solar thermal energy harvesting. *Sol. Energy Mater. Sol. Cells*, 137, 235–242.
10. Jianfa Zhang, Wei Liu, Zhihong Zhu, Xiaodong Yuan, and Shiqiao Qin (2014). Strong electric field enhancements and light matter interactions with all dielectric metamaterials based on split bar resonators, *Optics Express*, 22, 30889-30898.
11. G. V. Naik, J. Kim, and A. Boltasseva, (2011). Oxides and nitrides as alternative plasmonic materials in the optical range, *Optical Materials Express*, 1, 1090-1099.
12. S. Franzen (2008), Surface plasmon polaritons and screened plasma absorption in indium tin oxide compared to silver and gold, *The Journal of Physical Chemistry C*, 112, 6027-6032.
13. Johns, B., Chattopadhyay, S., & Mitra, J. (2021). Tailoring Infrared Absorption and Thermal Emission with Ultrathin-film Interferences in Epsilon-Near-Zero Media, *Adv Photonics Research*, 2100153, 1–9.
14. Vassant, S., Archambault, A., Marquier, F., Pardo, F., Gennser, U., Cavanna, A., Pelouard, J. L., & Greffet, J. J. (2012). Epsilon-near-zero mode for active optoelectronic devices. *Physical Review Letters*, 109(23), 1–5.
15. Rinnerbauer, V., Ndao, S., Yeng, Y. X., Chan, W. R., Senkevich, J. J., Joannopoulos, J. D., Soljačić, M., & Celanovic, I. (2012). Recent developments in high-temperature

- photonic crystals for energy conversion. *Energy and Environmental Science*, 5(10), 8815–8823.
16. Ning, Y., Wang, J., Ou, C., Sun, C., Hao, Z., Xiong, B., Wang, L., Han, Y., Li, H., & Luo, Y. (2020). NiCr–MgF₂ spectrally selective solar absorber with ultra-high solar absorptance and low thermal emittance. *Solar Energy Materials and Solar Cells*, 206.
 17. Danzi, S., Menétrey, M., Wohlwend, J., & Spolenak, R. (2019). Thermal Management in Ni/Al Reactive Multilayers: Understanding and Preventing Reaction Quenching on Thin Film Heat Sinks. *ACS Applied Materials and Interfaces*, 11, 42479–42485.
 18. Raman, A. P., Anoma, M. A., Zhu, L., Rephaeli, E., & Fan, S. (2014). Passive radiative cooling below ambient air temperature under direct sunlight. *Nature*, 515(7528), 540–544.
 19. Heo, S. Y., Lee, G. J., & Song, Y. M. (2022). Heat-shedding with photonic structures: radiative cooling and its potential. *Journal of Materials Chemistry C*, 10(27), 9915–9937.
 20. Wu, M., Shi, Y., Li, R., & Wang, P. (2018). Spectrally Selective Smart Window with High Near-Infrared Light Shielding and Controllable Visible Light Transmittance. *ACS Applied Materials and Interfaces*, 10(46), 39819–39827.
 21. Li, Z., Palacios, E., Butun, S., Kocer, H., & Aydin, K. (2015). Omnidirectional, broadband light absorption using large- area, ultrathin lossy metallic film coatings. *Scientific Reports*, 1–8.
 22. Dan, A., Jyothi, J., Chattopadhyay, K., Barshilia, H. C., & Basu, B. (2016). Spectrally selective absorber coating of WAIN/WAlON/Al₂O₃ for solar thermal applications. *Solar Energy Materials and Solar Cells*, 157, 716–726.
 23. Dan, A., Soum-Glaude, A., Carling-Plaza, A., Ho, C. K., Chattopadhyay, K., Barshilia, H. C., & Basu, B. (2019). Temperature- And Angle-Dependent Emissivity and Thermal Shock Resistance of the W/WAIN/WAlON/Al₂O₃-Based Spectrally Selective Absorber. *ACS Applied Energy Materials*, 2(8), 5557–5567.
 24. Jyothi, J., Chaliyawala, H., Srinivas, G., Nagaraja, H. S., & Barshilia, H. C. (2015). Design and fabrication of spectrally selective TiAlC/ TiAlCN/ TiAlSiCN/ TiAlSiCO/ TiAlSiO tandem absorber for higher temperature solar thermal power applications. *Solar Energy Materials and Solar Cells*, 140, 209–216.
 25. Raza, A., Alketbi, A. S., Devarapalli, R., Li, H., & Zhang, T. J. (2020). Refractory Ultrathin Nanocomposite Solar Absorber with Superior Spectral Selectivity and Thermal Stability. *Advanced Optical Materials*, 8(17), 1–9.
 26. Lin, K. Te, Lin, H., Yang, T., & Jia, B. (2020). Structured graphene metamaterial selective absorbers for high efficiency and omnidirectional solar thermal energy conversion. *Nature Communications*, 11(1), 1–10.
 27. Wu, Y., Hu, E. T., Cai, Q. Y., Wang, J., Wang, Z. Y., Tu, H. T., Wei, W. (2021). Enhanced thermal stability of the metal/dielectric multilayer solar selective absorber by an atomic-layer-deposited Al₂O₃ barrier layer. *Applied Surface Science*, 541, 148678.
 28. Jiang, X., Zhang, Z., Chen, D., Wen, K., & Yang, J. (2020). Tunable multilayer-graphene-based broadband metamaterial selective absorber. *Applied Optics*, 59(35), 11137.

29. Jian Wang, Zhikun Ren, Yi Luo, Zuoxu Wu, Yijie Liu, Shuaihang Hou, Xingjun Liu, Qian Zhang, and Feng Cao. High-Performance Spectrally Selective Absorber Using the ZrB₂-Based All-Ceramic Coatings (2021). *ACS Applied Materials and Interfaces*, 13(34), 40522–40530.
30. Niranjana, K., Kondaiah, P., Srinivas, G., & Barshilia, H. C. (2019). Optimization of W/WAISiN/SiON/SiO₂ tandem absorber consisting of double layer anti-reflection coating with broadband absorption in the solar spectrum region. *Applied Surface Science*, 496, 143651.
31. Liao, Q., Zhang, P., Yao, H., Cheng, H., Li, C., & Qu, L. (2020). Reduced Graphene Oxide-Based Spectrally Selective Absorber with an Extremely Low Thermal Emittance and High Solar Absorptance. *Advanced Science*, 7(8).
32. Tsai, T. K., Li, Y. H., & Fang, J. S. (2016). Spectral properties and thermal stability of CrN/CrON/Al₂O₃ spectrally selective coating. *Thin Solid Films*, 615, 91–96.
33. Park, C. S., & Lee, S. S. (2021). Vivid Coloration and Broadband Perfect Absorption Based on Asymmetric Fabry-Pérot Nanocavities Incorporating Platinum. *ACS Applied Nano Materials*, 4(4), 4216–4225.
34. Wang, H., Haechler, I., Kaur, S., Freedman, J., & Prasher, R. (2018). Spectrally selective solar absorber stable up to 900 °C for 120 h under ambient conditions. *Solar Energy*, 174, 305–311.
35. Shrestha, S., Wang, Y., Overvig, A. C., Lu, M., Stein, A., Dal Negro, L., & Yu, N. (2018). Indium Tin Oxide Broadband Metasurface Absorber. *ACS Photonics*, 5(9), 3526–3533.
36. Osgouei, A. K., Hajian, H., Serebryannikov, A. E., & Ozbay, E. (2021). Hybrid indium tin oxide-Au metamaterial as a multiband bi-functional light absorber in the visible and near-infrared ranges. *Journal of Physics D: Applied Physics*, 54(27).
37. Yildirim, D. U., Ghobadi, A., Soydan, M. C., Atesal, O., Toprak, A., Caliskan, M. D., & Ozbay, E. (2019). Disordered and Densely Packed ITO Nanorods as an Excellent Lithography-Free Optical Solar Reflector Metasurface. *ACS Photonics*, 6(7), 1812–1822.
38. Yoon, J., Zhou, M., Badsha, M. A., Kim, T. Y., Jun, Y. C., & Hwangbo, C. K. (2015). Broadband Epsilon-Near-Zero Perfect Absorption in the Near-Infrared. *Scientific Reports*, 5, 1–8.
39. Naik, G. V., Shalae, V. M., & Boltasseva, A. (2013). Alternative plasmonic materials: Beyond gold and silver. *Advanced Materials*, 25(24), 3264–3294.
40. Traylor Kruschwitz, J. D., & Pawlewicz, W. T. (1997). Optical and durability properties of infrared transmitting thin films. *Applied Optics*, 36(10), 2157.
41. Johns, B., Puthoor, N. M., Gopalakrishnan, H., Mishra, A., Pant, R., & Mitra, J. (2020). Epsilon-near-zero response in indium tin oxide thin films: Octave span tuning and IR plasmonics. *Journal of Applied Physics*, 127(4).
42. Wang, Y., Overvig, A. C., Shrestha, S., Zhang, R., Wang, R., Yu, N., & Dal Negro, L. (2017). Tunability of indium tin oxide materials for mid-infrared plasmonics applications. *Optical Materials Express*, 7(8), 2727.

43. Yi, F., Shim, E., Zhu, A. Y., Zhu, H., Reed, J. C., & Cubukcu, E. (2013). Voltage tuning of plasmonic absorbers by indium tin oxide. *Applied Physics Letters*, *102*(22).
44. Amin, R., Tahersima, M. H., Ma, Z., Suer, C., Liu, K., Dalir, H., & Sorger, V. J. (2018). Low-loss tunable 1D ITO-slot photonic crystal nanobeam cavity. *Journal of Optics (United Kingdom)*, *20*(5).
45. Karlsson, B., & Ribbing, C. G. (1982). Optical constants and spectral selectivity of stainless steel and its oxides. *Journal of Applied Physics*, *53*(9), 6340–6346.
46. Johnson, P. B., & Christy, R. W. (1974). Optical constants of transition metals. *Physical Review B*, *9*(12), 5056–5070.